Research Article

Collagen/heparan sulfate porous scaffolds loaded with neural stem cells improve neurological function in a rat model of traumatic brain injury

https://doi.org/10.4103/1673-5374.300458
Date of submission: March 4, 2020
Date of decision: April 15, 2020
Date of acceptance: August 10, 2020
Date of web publication: November 27, 2020

Jian Zhang[1, 2, #], Ren-Jie Wang[1, #], Miao Chen[3], Xiao-Yin Liu[4], Ke Ma[1, 2], Hui-You Xu[1, 2], Wu-Sheng Deng[1], Yi-Chao Ye[1, 2], Wei-Xin Li[2], Xu-Yi Chen[1, *], Hong-Tao Sun[1, *]

Graphical Abstract *Transplantation of the collagen/heparin sulfate scaffold that (C/H) combined with neural stem cells (NSCs) can effectively promote the recovery of neurological deficit after traumatic brain injury in rats*

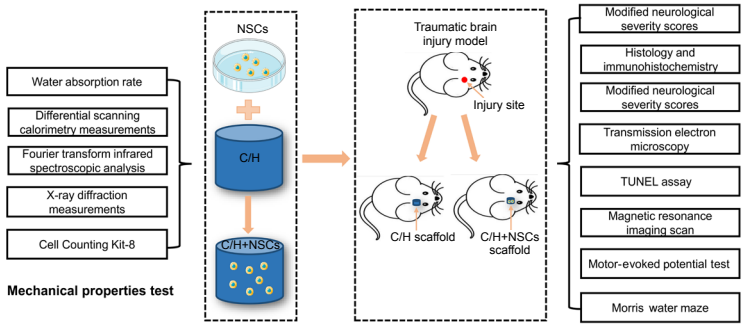

Abstract

One reason for the poor therapeutic effects of stem cell transplantation in traumatic brain injury is that exogenous neural stem cells cannot effectively migrate to the local injury site, resulting in poor adhesion and proliferation of neural stem cells at the injured area. To enhance the targeted delivery of exogenous stem cells to the injury site, cell therapy combined with neural tissue engineering technology is expected to become a new strategy for treating traumatic brain injury. Collagen/heparan sulfate porous scaffolds, prepared using a freeze-drying method, have stable physical and chemical properties. These scaffolds also have good cell biocompatibility because of their high porosity, which is suitable for the proliferation and migration of neural stem cells. In the present study, collagen/heparan sulfate porous scaffolds loaded with neural stem cells were used to treat a rat model of traumatic brain injury, which was established using the controlled cortical impact method. At 2 months after the implantation of collagen/heparan sulfate porous scaffolds loaded with neural stem cells, there was significantly improved regeneration of neurons, nerve fibers, synapses, and myelin sheaths in the injured brain tissue. Furthermore, brain edema and cell apoptosis were significantly reduced, and rat motor and cognitive functions were markedly recovered. These findings suggest that the novel collagen/heparan sulfate porous scaffold loaded with neural stem cells can improve neurological function in a rat model of traumatic brain injury. This study was approved by the Institutional Ethics Committee of Characteristic Medical Center of Chinese People's Armed Police Force, China (approval No. 2017-0007.2) on February 10, 2019.

Key Words: collagen; heparan sulfate; injury; neural stem cells; regeneration; repair; scaffold; traumatic brain injury; morris water maze; motor evoked potential; synapses; myelin sheaths

Chinese Library Classification No. R456; R741; Q81

Introduction

The treatment of traumatic brain injury (TBI) remains a major challenge around the world because of the brain's limited self-repair abilities after injury (Tam et al., 2014). Despite numerous efforts in recent years, no specific therapies can repair the injured site or reconnect injured neuronal circuits, likely because of complicated pathophysiological processes, cavity formation following brain tissue loss, and the poor

[1]Tianjin Key Laboratory of Neurotrauma Repair, Institute of Traumatic Brain Injury and Neuroscience, Characteristic Medical Center of Chinese People's Armed Police Force, Tianjin, China; [2]Graduate School, Logistics University of People's Armed Police Force, Tianjin, China; [3]Graduate School, Affiliated Hospital of Traditional Chinese Medicine, Xinjiang Medical University, Urumqi, Xinjiang Uygur Autonomous Region, China; [4]Graduate School, Tianjin Medical University, Tianjin, China

*Correspondence to: Hong-Tao Sun, PhD, zhangjian19237@126.com; Xu-Yi Chen, PhD, chenxuyi1979@126.com.
https://orcid.org/0000-0003-2076-3606 (Jian Zhang)
#Both authors contributed equally to this work.

Funding: *This work was supported by the National Natural Science Foundation of China, Nos. 11672332, 11932013 (both to XYC); the National Key Research and Development Plan of China, No. 2016YFC1101500 (to HTS); the Key Science and Technology Support Foundation of Tianjin of China, No. 17YFZCSY00620 (to HTS).*

How to cite this article: *Zhang J, Wang RJ, Chen M, Liu XY, Ma K, Xu HY, Deng WS, Ye YC, Li WX, Chen XY, Sun HT (2021) Collagen/heparan sulfate porous scaffolds loaded with neural stem cells improve neurological function in a rat model of traumatic brain injury. Neural Regen Res 16(6):1068-1077.*

self-repair capacity of nerve cells after TBI. Karlsson et al. (2000) suggested that neural stem cell (NSC) therapy is a safe and efficient method for replacing necrotic or damaged tissue after TBI. However, few studies have reported a clear therapeutic effect of NSCs delivered directly to the injury site after TBI. Transplanted exogenous NSCs are unable to effectively migrate to the local injury site because of a lack of extracellular matrix in this area, which results in very low NSC adhesion and proliferation rates (Cromer Berman et al., 2013). To enhance the targeted delivery of exogenous cells to the brain, biomaterial scaffolds loaded with stem cells have been widely tested as a potential treatment strategy to improve the ability of NSCs to promote recovery from neurological injury after TBI (Yan et al., 2019). However, an ideal biomaterial scaffold for TBI still needs to be developed.

Polysaccharides and proteins are promising natural polymers for the construction of biomaterial scaffolds, with the characteristics necessary for tissue engineering applications (Fischbach et al., 2009; Chen et al., 2012b). Previous studies have reported that polysaccharides can enhance stem cell expansion and differentiation via the fibroblast growth factor receptor 1 signaling pathway (Dombrowski et al., 2009; Smith et al., 2011). This signaling pathway plays an important role in mediating the dynamic process of stem cell differentiation into cells with neural lineages (Li et al., 2019b). Moreover, a variety of protein growth factors and chemokines can be combined with polysaccharides *in vivo* to prevent them from being affected by heat, acid, proteases, and other adverse factors, and to allow their involvement in various metabolic roles by activating specific signaling pathways in living organisms (Murakami et al., 2015). Polysaccharides are therefore often used to prepare neural tissue-engineered scaffolds for repairing nerve tissue defects, and can protect neurotrophic factors from proteolytic degradation, prolong their half-life, and maintain a balanced internal environment (Murakami et al., 2015; Chen et al., 2017).

Chitosan and heparan sulfate are widely used polysaccharides in tissue engineering. Chitosan is limited in that chemical cross-linking agents, such as genipin or glutaraldehyde, are needed for the preparation of chitosan scaffolds. Because most of these chemical cross-linking agents have certain cytotoxicity and high brittleness, biological scaffolds made using this method potentially risk compressing peripheral nerves (Skop et al., 2013). In contrast, biological scaffolds prepared using heparan sulfate can be induced by physical cross-linking methods, such as ultraviolet irradiation, thus avoiding the aforementioned adverse reactions (Chen et al., 2017). Heparan sulfate is a polysaccharide that makes up the neuronal basement membrane and extracellular matrix, and plays an important role in nerve fiber regeneration (Zhao et al., 2015). Additionally, heparan sulfate is involved in stem cell proliferation and differentiation through its interactions with various proteins (Nurcombe and Cool, 2007).

Studies have demonstrated that, in the process of biomaterial scaffold fabrication, a crosslinking reaction between collagen and heparan sulfate can enhance the mechanical strength of the scaffold by increasing the β-sheet content (Lu et al., 2007; Chen et al., 2017). Natural protein biomaterials, such as silk fibroin, gelatin, and collagen, are commonly used to make biological scaffolds in the field of tissue engineering. Collagen is a naturally occurring protein that is widely used in tissue engineering (Hu and Zhang, 2019). It is a common component in the extracellular matrix, and provides an appropriate microenvironment for nerve cell proliferation, differentiation, and metabolism (Zhang et al., 2019a). Similar to silk fibroin, collagen possesses low immunogenicity and excellent biodegradability and biocompatibility (Gentleman et al., 2003; Simionescu et al., 2006). Furthermore, collagen has a pivotal role in providing essential signals that influence cell activity (Yannas et al., 2010). We therefore hypothesized that the biological activity of NSCs might be improved if NSCs were co-cultured with collagen. However, as well as excellent biological properties, an ideal biomaterial scaffold should also have qualified mechanical properties, and collagen has poor physical properties and thermal stability (Cornwell et al., 2007). Some measures have consequently been suggested to make up the defects of collagen, for example, the cross-linking of collagen with heparan sulfate. In the present study, we focused mainly on the role of a collagen/heparan sulfate (C/H) scaffold loaded with NSCs in the repair of TBI-induced neurological deficits in rats.

Materials and Methods

Animals

To obtain the NSCs, two specific-pathogen-free Sprague-Dawley rats at 15 days of gestation were provided by the Academy of Military Medical Sciences, China [License No. SCXK (Jun) 2019-0006]. Furthermore, 48 male Sprague-Dawley rats (aged 12 weeks, weighing 200 ± 10 g) were included in the *in vivo* study. These animals were provided by the Academy of Military Medical Sciences, China [License No. SCXK (Jun) 2019-0010] and were kept in specific-pathogen-free conditions at the Animal Center of Tianjin Key Laboratory of Neurotrauma Repair. All animal research protocols and welfare were carried out in accordance with the Guide for the Care and Use of Animals of the Institutional Ethics Committee of Characteristic Medical Center of Chinese People's Armed Police Force, China (approval No. 2017-0007.2, approved on February 10, 2019). All experiments were designed and reported according to the ARRIVE (Animal Research: Reporting of In Vivo Experiments) guidelines.

NSC cultures and identification

Two pregnant rats were sacrificed with intraperitoneal injections of pentobarbital sodium (100 mg/kg; Solarbio Science & Technology Co., Ltd., Beijing, China). The bilateral cerebral cortices of the embryonic rats were immediately acquired under sterile conditions. The tissue was minced using microscissors and filtered through a 40 μm-sized mesh. A cell suspension was then prepared and primary NSCs were cultured as previously reported (Gao et al., 2015). The dissociated cells were seeded in T25 culture flasks (Corning Inc., Corning, NY, USA) at a density of 5×10^5 cells/cm^2 and cultured in growth medium, including serum-free Dulbecco's modified Eagle medium/F12 (Thermo Fisher Scientific, Waltham, MA, USA), 4 M glutamine (Thermo Fisher Scientific), 20 ng/mL basic fibroblast growth factor (Proteintech, Inc., Chicago, IL, USA), 20 ng/mL epidermal growth factor (Proteintech, Inc.), 2% B27 (Thermo Fisher Scientific) and 100 U/mL penicillin/streptomycin (Bioss Co. Ltd., Beijing, China), maintained at 37°C in a 5% CO_2 humidified incubator (XY-Bioscience, Shanghai, China). The dissociated cells gradually formed neurospheres after 1–3 days of culture in the growth medium. Sediment was discarded and the floating neurospheres were collected by centrifugation at 1466 × *g* at 4°C for 5 minutes. The neurospheres were then seeded into a new T25 culture flask with fresh growth medium. To acquire purified NSCs, the aforementioned passage process was repeated. When the NSCs were sub-cultured to the third generation, NSCs were identified by their morphological features under a light microscope (Leica Microsystems, Frankfurt, Germany) and with nestin [a marker of NSCs (Jiang et al., 2020)] immunofluorescence.

C/H scaffold preparation

Collagen was obtained from fresh bovine tendon using the acid swelling/pepsin digestion method (Shreiber et al., 2003). Briefly, fat and fascia were trimmed from the tendon and ground using a blender (Miulab, Hangzhou, Zhejiang, China). Subsequently, the residues were precipitated in 0.05 M Tris buffer solution for 24 hours. An acetic acid solution and

pepsin were then added to the solution, and the supernatant was collected. Next, 3.5 M NaCl solution was added to the supernatant to salt out the precipitation, followed by dialysis with deionized water at 4°C for 5 days. A previous study (Chen et al., 2017) demonstrated that a weight ratio of 20:1 (C/H) gives the best biocompatibility and mechanical properties for C/H scaffolds. The collagen and heparan sulfate (Nanjing Sai Hong Rui Biotechnology Co. Ltd., Nanjing, China) were therefore dissolved in 0.05 M acetic acid solution at this weight ratio and uniformly mixed using a magnetic stirrer (Wiggens, Berlin, Germany). The mixed solution was irradiated for 10 minutes with an ultraviolet lamp (365 nm, 18 W/cm^2) to induce the cross-linking reaction. The mixture was then freeze-dried with a vacuum freeze dryer for 2 days and immersed in 1% NaOH solution for 12 hours. Finally, the compound C/H material was repeatedly washed in deionized water. The samples were then cut into 2 × 2 × 2 mm^3 cylinders and sterilized using ^{60}Co (radiation dose 15 kGy).

A portion of the C/H scaffold (1 cm^2) was placed into the wells of a 12-well plate. For cell seeding, 100 µL of NSC suspension (1 × 10^7 cells/mL) was seeded onto the scaffolds, and the C/H scaffolds loaded with NSCs were incubated for 7 days at 37°C in a 95% air and 5% CO_2 humidified incubator. The medium was refreshed every 2 days. The C/H scaffolds co-cultured with NSCs were denoted as the C/H + NSCs group, and the NSCs cultured alone were denoted as the NSCs group.

Mechanical properties of the C/H scaffolds

Differential scanning calorimetry (DSC) measurements

DSC measurements were performed as previously described (Chen et al., 2012a). Approximately 10 mg C/H + NSC samples were heated to 400°C at a heating rate of 1°C /minute in an argon atmosphere. A DSC 1 calorimeter (Mettler Toledo, Zurich, Switzerland) was used to measure the phase transition temperature of the samples during heating.

X-ray diffraction measurements

The crystallization behavior of C/H + NSC samples was measured using an X-ray diffractometer (Malvern Panalytical BV, Eindhoven, Netherlands) over the 2 theta range from 5° to 90° at a scanning rate of 5°/minute.

Fourier-transform infrared spectroscopic analysis

The C/H + NSC samples were analyzed using a Nicolet Nexus 870 infrared spectrometer (Thermo Fisher Scientific). The Fourier-transform infrared spectroscopic spectra were analyzed at a range of 4000–600 cm^{-1}, with a resolution of 4.0 cm^{-1}.

Porosity measurement

Dry scaffolds were degassed in anhydrous ethanol for 5 minutes until no bubbles escaped from the samples, and the volume of anhydrous ethanol was denoted as V_a. The volume of anhydrous ethanol was recorded before (V_b) and after (V_c) removing the wet scaffolds. The porosity of the scaffold was calculated according to the following formula (Zeng et al., 2015): porosity (%) = $(V_a - V_c)/(V_b - V_c) \times 100$.

Water absorption rate

The weight of the freeze-dried scaffold was recorded as M_a. The scaffold was then immersed in 0.01 M phosphate-buffered saline (PBS) at 37°C for 24 hours before being dried rapidly with filter paper. The weight (M_b) was then recorded. The water absorption rate of the scaffold was calculated according to the following formula (Zeng et al., 2015): water absorption rate = $(M_a - M_b)/M_b \times 100$.

Assessment of NSC morphology, viability, and proliferation

The adhesion and morphology of NSCs in the C/H + NSC samples were observed under a scanning electron microscope (SEM; Hitachi, Tokyo, Japan). Briefly, the C/H + NSC samples were successively fixed with 2% glutaraldehyde (Shandong Forte Disinfection Products Co. Ltd., Dezhou, Shandong, China) and 1% osmium tetroxide (Sigma-Aldrich, St. Louis, MO, USA). The samples were then dehydrated with a gradient of acetone, rapidly frozen to the critical point by liquid nitrogen, and freeze-dried for 12 hours. Finally, the C/H + NSC samples were coated with gold, and the adhesion and morphology of the NSCs were observed under the SEM. Simultaneously, different regions were randomly selected and the pore diameters of the C/H scaffold were measured under the SEM.

Cell viability was measured using a Cell Counting Kit-8 (CCK-8) (Sigma-Aldrich) at 1, 3, 5, and 7 days after seeding NSCs. For this experiment, 100 µL of NSC suspension (1 × 10^7 cells/mL) was seeded to the C/H scaffold in 96-well plates and incubated at 37°C in a humidified incubator containing 5% CO_2. The medium was refreshed every 2 days. According to the manufacturer's instructions, 30 µL CCK-8 was added to each well and stirred. The samples were then incubated for 4 hours at 37°C in a 5% CO_2 humidified incubator. Finally, the reaction solutions (300 µL) were transferred to a 96-well plate. The absorbance of each well at 450 nm was measured by a Synergy 2 multi-mode microplate reader (BioTek, Winooski, VT, USA).

TBI model and scaffold transplantation

Forty-eight rats were randomly divided into four groups: sham (n = 12), TBI (n = 12), C/H (n = 12; C/H scaffold implantation after TBI), and C/H + NSCs (n = 12; C/H + NSC implantation after TBI). The rat model of TBI was prepared using the controlled cortical impact (CCI) method (eCCI Model 6.3; VCU, Richmond, VA, USA) as previously reported (Gao et al., 2015). Briefly, rats were anesthetized by intraperitoneal injection of pentobarbital sodium (50 mg/kg) and immobilized on a stereotactic frame. A 5 mm bony window was drilled in the right parietal region of the skull, 2 mm posterior to the coronal suture and 4 mm lateral to the sagittal suture. Moderate brain injury was induced with a 2 mm diameter cylinder in rats, with an impact velocity of 4.5 m/s, a depth of 2.0 mm, and a residence time of 120 ms. The rats in the sham group were not subjected to an impact.

For the C/H and C/H + NSCs groups, a 2 mm^3 C/H scaffold or C/H + NSC sample, respectively, was transplanted into the cavity after TBI.

Morris water maze test

To evaluate spatial learning and memory, the morris water maze (MWM) test was performed from 31–37 days after injury, as previously reported (Yang et al., 2014). The MWM test included the spatial learning stage and the spatial memory stage. In the spatial learning stage, each rat (n = 8 per group) was released into a circular pool filled with a mixture of water and black ink (50 cm deep), and were trained to find a submerged platform and remain there for 2 seconds. If the rats failed to arrive at the platform within 60 seconds, they were provided with a stationary array of prominent maze cues and remained in the pool for 20 seconds. The spatial learning experiments were performed for 6 consecutive days, and the escape latency (the time taken to find the hidden platform) was recorded. The spatial memory experiment was performed on day 37, when the platform was removed from the maze. The quadrant dwell time (percentage of total time spent in quadrant IV) and platform crossings (the number of times the platform region was crossed) were recorded. Swimming patterns and parameters were collected and analyzed using an automatic tracking system (Ethovision 2.0, Noldus, Venlo, the Netherlands).

Motor evoked potential test

The motor evoked potential (MEP) test was performed at 2 months after injury to analyze differences in motor function between the left and right limbs of each rat as a

result of damage to the cerebral motor cortex (Kim and Han, 2017; Jiang et al., 2018). First, rats were anesthetized by intraperitoneal injection of pentobarbital sodium (50 mg/kg). The recording electrodes were then inserted into the belly of the extensor carpi radialis of both forelimbs and the posterior tibial nerve of both hindlimbs. Next, the ground electrodes were inserted into the root of the tail, and the stimulating electrodes were located at the contralateral motor cortex, with the center taken as 2 mm posterior to the coronal suture and 4 mm lateral to the sagittal suture (Khatoun et al., 2019). The electrophysiology parameters were as follows: stimulation voltage 46 V, pulse width 0.2 ms, and stimulus frequency 1 Hz. The largest peak-to-peak amplitude and the earliest latency of MEP were recorded using evoked potential equipment (Nicolet; Thermo Fisher Scientific).

Magnetic resonance imaging

T2-weighted magnetic resonance imaging (MRI) was performed under general anesthesia at 1 month after injury to assess structural changes in the brain, using a 3.0 T MRI system (MAGNETOM Verio, Siemens, Berlin, Germany). T2-weighted images were obtained using the following sequence parameters: repetition time 3200 ms, echo time 83 ms, rapid imaging with refocused echoes (RARE) factor 10, field of view 19.2 mm × 19.2 mm, matrix size 320 × 320, number of acquisitions 20, and slice thickness 2 mm. Apparent diffusion coefficient (ADC) values were separately analyzed by two researchers using a double-blind method. The region of interest to be measured was located in the cortex, around the injury site. According to the results of brain tissue morphology displayed on T2-weighted images, three measurement points were randomly selected from the corresponding ADC images. The mean value across three measurement points was calculated and denoted as the ADC value of the region.

Neurological function observation

Modified neurological severity scores (mNSS) were used to assess neurological function changes in rats (n = 10 in each group) at 1, 5, 10, 15, 20, 25, 30, 35, 40, and 45 days after injury. The mNSS scores were graded on an 18-point scale that included reflex, motor, sensory, and balance tests. The detailed procedures were carried out according to a previous report (Wen et al., 2017). Briefly, each rat was trained and assessed before CCI to determine the normal score (0). The neurological scores were then calculated by blinded testers at different time points after CCI. A higher mNSS indicated more severe sensory and motor functional deficits.

Histology and immunohistochemistry

Animals were sacrificed at 2 months after CCI with an overdose of chloral hydrate and were then perfused with 200 mL normal saline and 200 mL 4% paraformaldehyde. For the histomorphological examinations, brain tissue was fixed with 4% paraformaldehyde for 24 hours and sliced into 5 μm-thick sections on an automatic paraffin slice system (MEDITE, Hanover, Germany). Hematoxylin and eosin staining was performed to observe morphological changes and local tissue repair at the injury site. The cavity volume was measured using ImageJ (National Institutes of Health, Bethesda, MD, USA) and computed using the following equations: $n = 1 - 8 \sum (A_n + A_n + 1) \times d/2$ (A = area, d = distance between sections) and % lesion volume = $[(V_0 - V_1) / (V_0)] \times 100$ (V_0 = contralateral (uninjured) hemisphere volume, V_1 = ipsilateral (injured) hemisphere volume).

Nissl staining and silver staining were also performed to analyze neuron and nerve fiber regeneration (Cheng et al., 2018). Furthermore, 5-bromo-2′-deoxyuridine (BrdU) staining was performed to identify newborn nerve cells (Kee et al., 2002). Four rats from each group were intraperitoneally injected with BrdU (100 mg/kg; Cat# abs811906; Absin, Shanghai, China) for 10 consecutive days after injury to label proliferating cells. For BrdU immunohistochemical staining, the brain sections were incubated with 3% H_2O_2 at room temperature for 10 minutes, and were then washed three times with PBS for 5 minutes each. Next, the slides were incubated for 12 hours at 4°C with 100 μL rabbit anti-BrdU (1:100; Cat# bs-0489R-1; Bioss, Beijing, China), rinsed with PBS, incubated at 37°C for 1 hour with biotinylated sheep anti-rabbit IgG (1:200; Cat# PAB10842-E; Abnova, Wuhan, China), rinsed with PBS, and developed with 3,3′-diaminobenzidine. The slides were then stained with hematoxylin for 2–3 minutes, dehydrated, cleared, sealed, and differentiated with a hydrochloric acid/ethanol solution. Six random fields were visualized from each section under a DM IL inverted contrasting microscope (Leica Microsystems, Frankfurt, Germany). The numbers of BrdU-positive cells in each field of view were calculated for each group.

Terminal deoxynucleotidyl transferase dUTP nick-end labeling assay

Brain tissue sections were prepared as previously described (Neher et al., 2014; Li et al., 2019a). Before staining, sections were dewaxed using a Drift baking machine (Yu De Co., Guangzhou, Guangdong Province, China) and dehydrated using graded ethanol. The apoptotic cells around the injury site were then detected using a terminal deoxynucleotidyl transferase dUTP nick-end labeling (TUNEL) detection kit (Roche, Basel, Switzerland) according to the manufacturer's instructions. The 4′,6-diamidino-2-phenylindole (DAPI) was incubated in dark for 5 minutes to stain cell nucleus. Apoptotic neuronal cells were visualized under a fluorescence microscope (Leica Microsystems). Six fields were randomly selected on each slide for the quantification of TUNEL- and DAPI-stained cells by two researchers blinded to the experiment.

Transmission electron microscopy

Rats were anesthetized by intraperitoneal injection of pentobarbital sodium (50 mg/kg) at 2 months after injury. The brains were rapidly isolated and the lesioned area was diced into 1 × 1 × 1 mm^3 cubes on ice. Samples were fixed with 2% glutaraldehyde for 4 hours and washed with 1/15 M PBS for 15–30 minutes. The samples were then fixed with 1% osmium tetroxide for 2 hours and washed with 1/15 M PBS for 15–30 minutes. Next, the samples were dehydrated through graded ethanols and embedded in epon. An ultramicrotome (Leica UCT, Frankfurt, Germany) was used to make 70–90 nm-thick sections. These ultrathin sections were stained with uranyl acetate and lead acetate, and tissue ultrastructure was observed among the four rat groups using transmission electron microscopy (TEM). The synaptic curvature, cleft width, number of myelinated axons per 1000 μm^2, diameter of myelinated axons, and myelinated thickness were analyzed in each group.

Statistical analysis

The data are expressed as the mean ± standard deviation (SD). Statistical comparisons between groups were conducted using the two-sample t-test, or the one-way analysis of variance followed by the Student-Newman-Keuls test. A P-value < 0.05 indicated a statistically significant difference. All calculations were carried out using SPSS software (version 22.0; IBM, Armonk, NY, USA).

Results

Characterization of the C/H scaffold

Under the SEM, the pores of the C/H scaffold were evenly distributed and well interconnected (**Figure 1A**). The pore diameter was 265.4 ± 63.5 μm, with a range of 200–400 μm; pore diameters in this range are suitable for cell proliferation and adhesion (Bose et al., 2012). The NSCs were spherical (**Figure 1B**) and the expression of surface-bound nestin on

NSCs was determined using immunofluorescence (**Figure 1C**). Using light microscopy, NSCs were observed to be closely attached to the surface of the C/H scaffold. Some NSCs extended pseudopodia to contact each other, which even extended into the interior of pores (**Figure 1D** and **E**). Using SEM, NSCs were observed to gather together and were tightly attached to the C/H scaffold (**Figure 1F**). The CCK-8 results demonstrated that the C/H scaffold was not cytotoxic for NSC growth (**Figure 1G**). Compared with the NSCs group, the optical density values of the C/H + NSCs group markedly increased ($P < 0.05$) over time, again indicating that NSCs successfully proliferated on this scaffold. Additionally, the C/H + NSC samples had excellent physical properties. The C/H scaffold had higher porosity and lower water absorption capabilities than the pure collagen scaffold ($P < 0.05$; **Figure 1H** and **I**). In the Fourier-transform infrared spectroscopic analysis of the C/H materials (**Figure 1J**), the frequencies at 3294.78 cm^{-1}, 1632.43 cm^{-1}, 1547.77 cm^{-1}, and 1031.19 cm^{-1} were correlated with the stretching vibrations of the C-H bond, C=O bond in COOH, NH_2 double bonds, N-H bond, or C-N bond, respectively. In the X-ray diffraction analysis (**Figure 1K**), a sharp diffraction peak was observed at 21.82°, indicating that crystallization of the materials increased when heparan sulfate was added to collagen to generate a cross-linking reaction. The DSC image (**Figure 1L**) revealed that the heat flow of the C/H scaffold gradually changed with the constantly rising temperature. Three endothermic peaks appeared in the samples, at 113.95°C, 226.03°C, and 261.15°C. This result indicates that the samples begin to absorb thermal energy and decompose at these high temperatures.

C/H + NSC therapy enhances the recovery of neurological motor functions

The MWM test was carried out 1 month after injury to evaluate the influence of C/H + NSC transplantation on spatial cognitive function. In the spatial learning stage, the escape latencies in all groups were significantly reduced with training. In particular, C/H + NSC transplantation markedly promoted a decrease in escape latencies, while the escape latencies in the TBI group were the longest (**Figure 2A**). Student–Newman–Keuls test results revealed significant differences in escape latencies among the four groups at each time point (**Figure 2C**). The results of the MWM test indicated that the C/H + NSC group took a similar amount of time to reach the submerged platform as the sham group ($P > 0.05$), while the escape latencies were markedly lower in the C/H + NSCs group compared with the TBI and C/H groups (C/H + NSCs *vs*. C/H, $P < 0.05$; C/H + NSCs *vs*. TBI, $P < 0.01$). In the spatial memory stage of the MWM, the quadrant dwell time and platform crossings were recorded. The number of platform crossings was higher and the quadrant dwell time was longer in the C/H + NSCs group compared with the TBI and C/H groups (**Figure 2B**). The Student–Newman–Keuls test demonstrated that quadrant dwell time and platform crossings were significantly higher in the C/H + NSCs group (C/H + NSCs group *vs*. C/H group, $P < 0.05$; C/H + NSCs group *vs*. TBI group, $P < 0.01$), while the rats in the sham group spent the most time in the target quadrant and had the largest numbers of platform crossings (sham group *vs*. C/H group, $P < 0.05$; sham group *vs*. TBI group, $P < 0.01$) (**Figure 2D** and **E**). This *in vivo* experiment indicates that C/H + NSC transplantation can reverse cognitive impairment after brain injury.

The MEP tests were carried out 2 months after injury (**Figure 2F**), and a statistical analysis of the latencies and amplitudes was conducted among the four groups (**Figure 2G–I**). For the MEP amplitudes (**Figure 2G**), the representative MEP waveform of the left limbs almost disappeared in the TBI group. Compared with the sham group, the MEP amplitudes of the left limbs in the other three groups were lower ($P < 0.05$, *vs*. NSCs group; $P < 0.05$, *vs*. C/H + NSCs group; $P < 0.01$, *vs.* TBI group). Additionally, the MEP amplitudes of the left limbs in the C/H + NSCs and C/H groups were higher than those in the TBI group ($P < 0.01$, *vs.* C/H + NSCs group; $P < 0.05$, *vs*. C/H group), and the MEP amplitudes of the left limbs in the C/H + NSCs group were higher than those in the C/H group ($P < 0.05$). Similar differences were observed in the MEP latencies (**Figure 2H**). The MEP latencies of the left limbs in the sham group were the shortest among the four groups ($P < 0.05$, *vs*. C/H + NSCs group; $P < 0.05$, *vs*. C/H group; $P < 0.01$, *vs*. TBI group), followed by the C/H + NSCs group, which had shorter MEP latencies of the left limbs than the C/H and TBI groups ($P < 0.05$, *vs*. C/H group; $P < 0.01$, *vs*. TBI group). The MEP latencies of the left limbs in the TBI group were the longest. There were no significant differences in MEP latency or amplitude of the right limbs among the four groups ($P > 0.05$).

The mNSS testing was carried out to assess behavioral changes. As shown in **Figure 2I**, the rats in the TBI, C/H + NSCs, and C/H groups obtained high scores on day 1 after CCI, while the mNSS scores were close to 0 in the sham group. Subsequently, the mNSS scores of the TBI, C/H + NSCs, and C/H groups had a decreasing trend. Statistical analysis revealed that C/H + NSCs transplantation in the injury site led to marked improvements in sensorimotor function (as measured by mNSS scores) compared with the TBI and C/H groups at 10 days after CCI ($P < 0.05$, *vs*. C/H group; $P < 0.01$, *vs.* TBI group).

C/H + NSC therapy decreases injury volume and promotes the regeneration of damaged nervous tissue

Hematoxylin and eosin staining of brain slices was carried out at 2 months after CCI to investigate whether or not C/H + NSC therapy decreased tissue loss. Nerve cells in the sham group had homogeneous cytoplasm with no pathological changes such as cell shrinkage, dark staining, or morphological changes. In the TBI group, a large number of nerve cells were lost in the injury site, but the number of newborn nerve cells was small. Many nerve cells around the lesion site developed nuclear wrinkling and deformation and had uneven cytoplasm. In the C/H and C/H + NSCs groups, large numbers of newborn nerve cells were observed at the injury site. Pathological changes, such as cell shrinkage and morphological changes, were observed in both groups. The pathological changes in the C/H + NSCs group were less severe than those in the TBI group (**Figures 3A–D2**). At 2 months after injury, the lesion volume in the C/H + NSCs group was markedly lower compared with the C/H and TBI groups (C/H + NSCs group *vs.* C/H group, $P < 0.05$; C/H + NSCs group *vs*. TBI group, $P < 0.01$), and C/H scaffold therapy led to significantly smaller lesion volumes compared with the TBI group ($P < 0.05$) (**Figure 3O**). Similar changes were noted from the overall observation of brain tissue at 2 months after CCI among the four groups (**Figure 3E**). These results suggest that C/H + NSCs therapy is beneficial for promoting the recovery of cavity lesions after TBI.

Silver staining results (**Figure 3F–I**) revealed nerve fiber changes at the injury site among the four groups. Representative sections demonstrated that nerve fibers were evident in the perilesional region and injury site in the C/H + NSCs and C/H groups (**Figure 3G** and **H**). The C/H + NSCs group had the highest density and the largest distribution scope of nerve fibers in the perilesional region and injury site compared with the C/H and TBI groups (C/H + NSCs group *vs*. C/H group, $P < 0.05$; C/H + NSCs group *vs.* TBI group, $P < 0.01$), followed by the C/H group (C/H group *vs.* TBI group, $P < 0.05$). Additionally, the Nissl staining results (**Figure 3J–M**) showed Nissl body changes in the perilesional region and injury site in each group. There were larger numbers of Nissl bodies in the perilesional region and injury site in the C/H + NSCs group than in the TBI and C/H groups (C/H + NSCs group *vs*. C/H group, $P < 0.05$; C/H + NSCs group *vs.* TBI group, $P < 0.01$). Furthermore, the TBI group had the lowest density and distribution scope in the perilesional region and injury site among the four groups (TBI group *vs*. C/H group, $P < 0.05$).

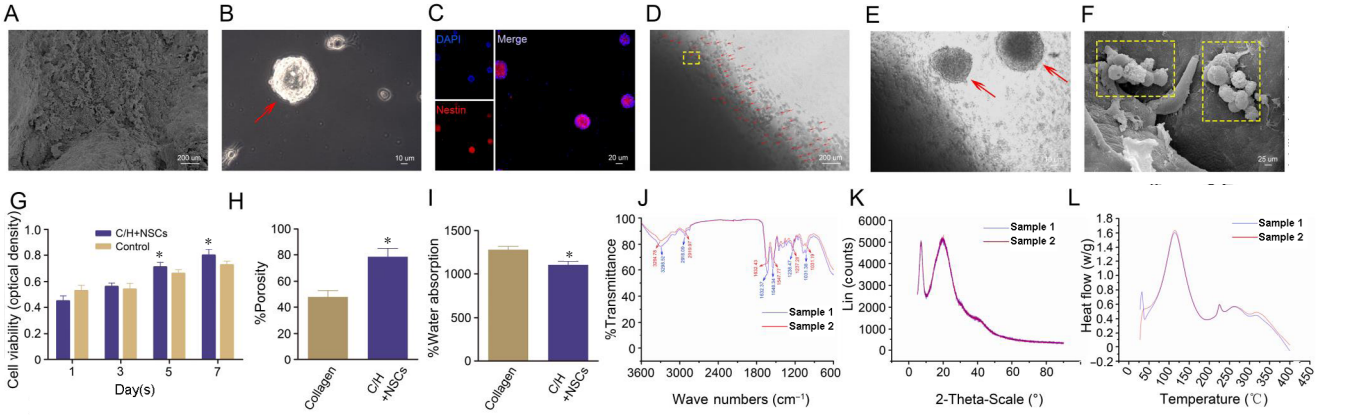

Figure 1 | **Mechanical properties of C/H scaffold and identification of NSCs.**
(A) Microcellular structure of the C/H scaffold under a scanning electron microscope. (B) The morphology of NSCs (arrow) under optical microscopy. (C) Merged immunofluorescence image of NSCs, with nuclei in blue (DAPI) and nestin-positive cells in red. Nestin: an intermediate filament protein specifically expressed in neuroepithelial stem cells. (D) General view of the C/H scaffold co-cultured with NSCs under optical microscopy. Red arrows indicate NSCs. (E) Magnified image of the yellow box in D. (F) Yellow dotted frame shows that the NSCs gathered together in the micropores of the C/H scaffold. (G) Comparison of the CCK-8 assay between NSCs co-cultured with or without the C/H scaffold. The control group was composed of NSCs co-cultured without the C/H scaffold. (H) Comparison of porosity between the C/H scaffold and collagen scaffold. (I) Comparison of water absorption between the C/H scaffold and collagen scaffold. (J) Fourier-transform infrared spectroscopic image of two C/H scaffolds from different batches. Sample 1 represents the C/H scaffolds that were tested in the first batch; sample 2 represents the C/H scaffolds that were tested in the second batch. (K) X-ray diffraction image of two C/H scaffolds from different batches. (L) Differential scanning calorimetry image of two C/H scaffolds from different batches. Scale bars: 200 μm in A and D, 10 μm in B and E, 25 μm in F, 20 μm in C. Data are expressed as the mean ± SD. *$P < 0.05$, *vs.* control group (two-sample *t*-test). CCK-8: Cell Counting Kit-8; C/H: collagen/heparan sulfate; DAPI: 6-diamidino-2-phenylindole; NSC: neural stem cell.

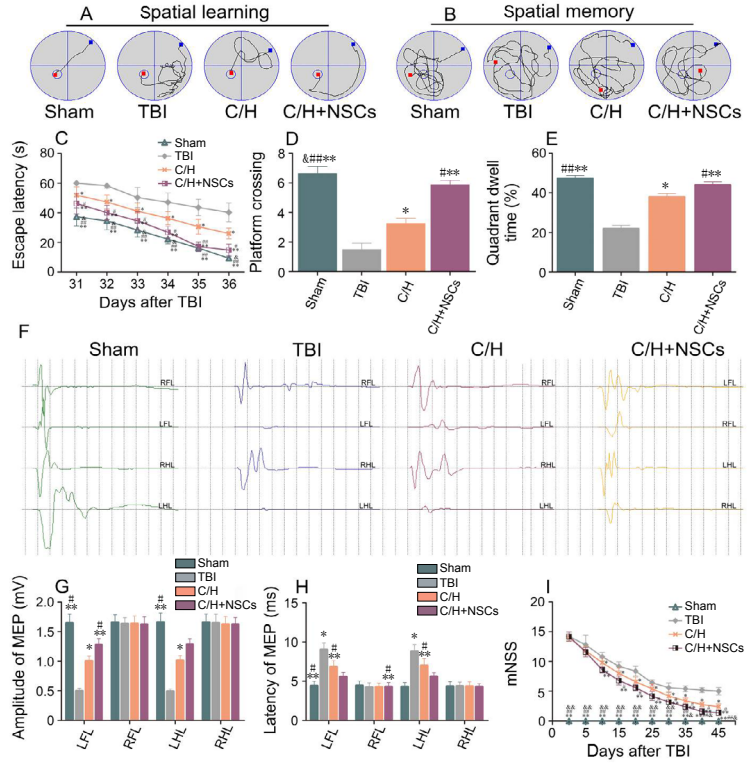

Figure 2 | **Transplantation of C/H + NSCs significantly enhances the recovery of neurological motor function after TBI.**
(A) Representative swimming tracks during the spatial learning task. Compared with the TBI and C/H groups, the C/H + NSCs group took less time to find the submerged platform. (B) Representative swimming tracks during the spatial memory task. The C/H + NSCs group had more platform crossings and spent more time in the target quadrant compared with the TBI and C/H groups. The blue dots indicate the initial position and the red dots indicate the target position. (C) The mean escape latency was analyzed at each time point during the spatial learning task. (D) Average number of platform crossings among the four groups during the spatial memory task (within 60 seconds). (E) Average time spent in the target quadrant among the four groups during the spatial memory task. (F) Representative MEP images among the four groups at 2 months after TBI. (G) Statistical comparison of MEP amplitudes among the four groups. (H) Statistical comparison of MEP latencies among the four groups. (I) mNSS at 1, 5, 10, 15, 20, 25, 30, 35, 40, and 45 days after TBI among the four groups. Data are expressed as the mean ± SD. *$P < 0.05$, **$P < 0.01$, *vs.* TBI group; #$P < 0.05$, *vs.* C/H group; &$P < 0.05$, &&$P < 0.01$, *vs.* C/H + NSCs group (one-way analysis of variance followed by the Student-Newman-Keuls test). C/H: Collagen/heparan sulfate; LFL: left forelimb; LHL: left hindlimb; MEP: motor evoked potential; mNSS: Modified Neurological Severity Score; NSC: neural stem cell; RFL: right forelimb; RHL: right hindlimb; TBI: traumatic brain injury.

As shown in **Figure 4**, the numbers of BrdU-positive cells per field at the injury site were higher in the C/H and C/H + NSCs groups than in the TBI group ($P < 0.05$, *vs.* C/H group; $P < 0.01$, *vs.* C/H + NSCs group). Additionally, the C/H + NSCs group had more BrdU-positive cells than the C/H group ($P < 0.05$).

C/H + NSC therapy improves the absorption of hematoma after TBI

The MRI T2-weighted images demonstrated that C/H + NSC transplantation after CCI had positive therapeutic effects, enhancing hematoma absorption and promoting improvements in intracranial conditions (**Figure 3N**). The edema volume was noticeably smaller in the C/H + NSCs group than in the other three groups. The TBI group displayed marked subcortical hyperintensities, induced by trauma-associated hydrocephalus, 1 month after brain injury. In addition, compared with the sham group, ADC values were markedly higher in the other three groups (**Figure 3P**). The ADC values of the C/H + NSCs and C/H groups were significantly higher than those of the TBI group (TBI group *vs.* C/H group, $P < 0.05$; TBI group *vs.* C/H + NSCs group, $P < 0.01$). Moreover, the ADC values of the C/H + NSCs group were lower than those of the C/H group (C/H group *vs.* C/H + NSCs group, $P < 0.05$).

C/H + NSC therapy promotes the rehabilitation of injured synapses and myelin sheaths

Using TEM, a representative series of ultrastructural micrographs demonstrating synapses and myelin sheaths at the injury site is shown in **Figure 5**. The synapses in the sham group had distinct presynaptic membranes, postsynaptic

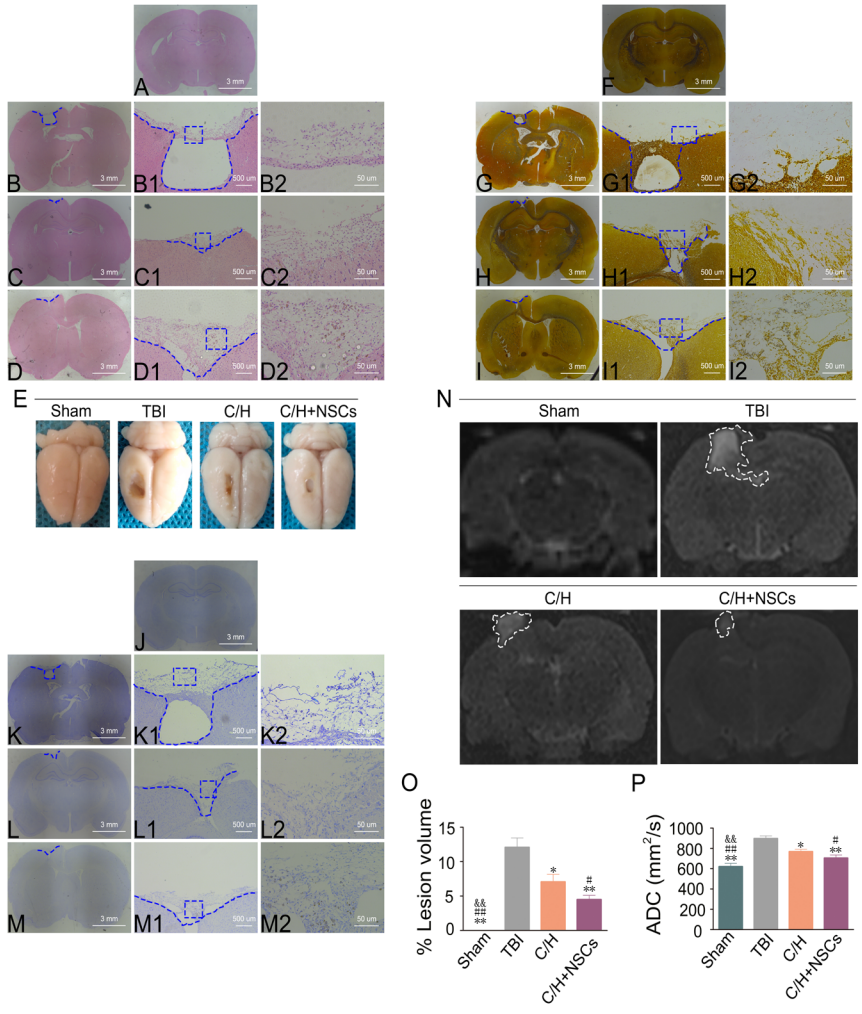

Figure 3 | Transplantation of C/H + NSCs significantly improves histomorphology at the transplant site after TBI.

(A) Representative H&E-stained brain slices showing the recovery of the lesion cavity after TBI on a single section in the sham (A), TBI (B–B2), C/H (C–C2), and C/H + NSCs (D–D2) groups. The cytoplasm of nerve cells in the sham group was homogeneous, without any pathological changes. A large number of nerve cells were lost at the lesion site in the TBI group. In the C/H and C/H + NSCs groups, a large number of newborn nerve cells were observed in the lesion. There were more newborn nerve cells in the C/H + NSCs group than in the C/H group. (E) A general observation of the brain tissue in each group at 2 months after surgery. The lesion cavity volume in the C/H + NSCs group was significantly smaller than in the C/H and TBI groups, and the cavity volume in the C/H group was significantly smaller than that in the TBI group. Red arrows indicate the injury site after controlled cortical impact injury. White dotted lines indicate the extent of the edema region. (F–I) Representative silver-stained brain sections showing nerve fiber changes in the perilesional region after TBI in a single section in the sham (F), TBI (G–G2), C/H (H–H2), and C/H + NSCs (I–I2) groups. (J–M) Representative Nissl-stained brain slices showing Nissl body changes in the perilesional region after TBI in a single section in the sham (J), TBI (K–K2), C/H (L–L2), and C/H + NSCs (M–M2) groups. The C/H + NSCs group had a higher density and larger distribution scope of nerve fibers, and had more Nissl body changes in the damaged area and perilesional region compared with the C/H and TBI groups. Blue dotted lines indicate the extent of the damaged area. Blue dotted frames indicate local magnification of the area of interest. (N) MRI T2-weighted images at 1 month after injury among the four groups. In the sham group, rat brain tissue was integral, without hematoma. Varying degrees of subcortical edema existed in the TBI, C/H, and C/H + NSCs groups. (O) Quantitative analysis of the full lesion volumes. (P) ADC analysis in the injury site. Data are expressed as the mean ± SD. $*P < 0.05$, $**P < 0.01$, *vs.* TBI group; $\#P < 0.05$, $\#\#P < 0.01$, *vs.* C/H group; $\&\&P < 0.01$, *vs.* C/H + NSCs group (one-way analysis of variance followed by the Student-Newman-Keuls test). Scale bars: 3 mm in A–D and F–M, 500 μm in B1–D1 and G1–M1, 25 μm in B2–D2 and G2–M2. ADC: Apparent diffusion coefficient; C/H: collagen/heparan sulfate; H&E: hematoxylin & eosin; MRI: magnetic resonance imaging; NSC: neural stem cell; TBI: traumatic brain injury.

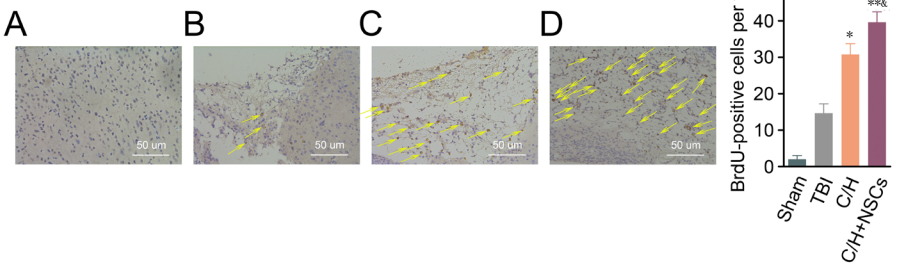

Figure 4 | Transplantation of C/H + NSCs significantly increases BrdU immunohistochemistry at the transplant site after TBI.

(A–D) BrdU immunohistochemistry in the injury site. (A) Sham group; (B) TBI group; (C) C/H group; (D) C/H + NSCs group. The number of BrdU-positive cells per field at the injury site was much smaller in the TBI group than in the C/H and C/H + NSCs groups, and the C/H + NSCs group had more BrdU-positive cells than the C/H group. Yellow arrows indicate BrdU-labeled cells. Scale bars: 50 μm in A–D. (E) Quantitative BrdU immunoreactivity among the four groups. Data are expressed as the mean ± SD. $*P < 0.05$, $**P < 0.01$, *vs.* TBI group; $\&P < 0.05$, *vs.* C/H group (one-way analysis of variance followed by the Student-Newman-Keuls test). BrdU: 5-Bromo-2′-deoxyuridine; C/H: collagen/heparan sulfate; NSC: neural stem cell; TBI: traumatic brain injury.

membranes, synaptic clefts, and synaptic interface curvature (**Figure 5E**). There were many synaptic vesicles in the presynaptic elements, and many dense materials attached to postsynaptic elements. The synapses in the other three groups showed unclear ultrastructure, with fused presynaptic and postsynaptic membranes, heterogeneous postsynaptic densities, and different synaptic cleft widths (**Figure 5F–H**). Quantitatively, the ultrastructure of the synaptic interface curvature was significantly increased and the synaptic cleft was significantly decreased in the C/H + NSCs group compared with the TBI and C/H groups (C/H + NSCs group *vs.* C/H group, $P < 0.05$; C/H + NSCs group *vs.* TBI group, $P < 0.01$) (**Figure 5L** and **M**). We also analyzed ultrastructural changes in myelin sheaths among the four groups (**Figure 5A–D**). Compared with the C/H and TBI groups, the myelinated axon diameter, myelinated thickness, and number of myelinated axons were significantly increased in the C/H + NSCs group (C/H + NSCs group *vs.* C/H group, $P < 0.05$; C/H + NSCs group *vs.* TBI group, $P < 0.01$) (**Figure 5I–K**). These results suggest that C/H + NSC transplantation after TBI promotes the rehabilitation of injured myelin sheaths and synapses.

TUNEL staining was performed at 2 months after brain injury to detect nerve cell survival and apoptosis (**Figure 6**). The numbers of TUNEL-positive cells at the injury site were significantly lower in the C/H and C/H + NSCs groups compared with the TBI group ($P < 0.05$, *vs.* C/H group; $P < 0.01$, *vs.* C/H + NSCs group). Moreover, the C/H + NSCs group contained fewer TUNEL-positive cells than the C/H group ($P < 0.05$). These results demonstrate that C/H + NSCs transplantation after TBI prevents apoptosis of nerve cells.

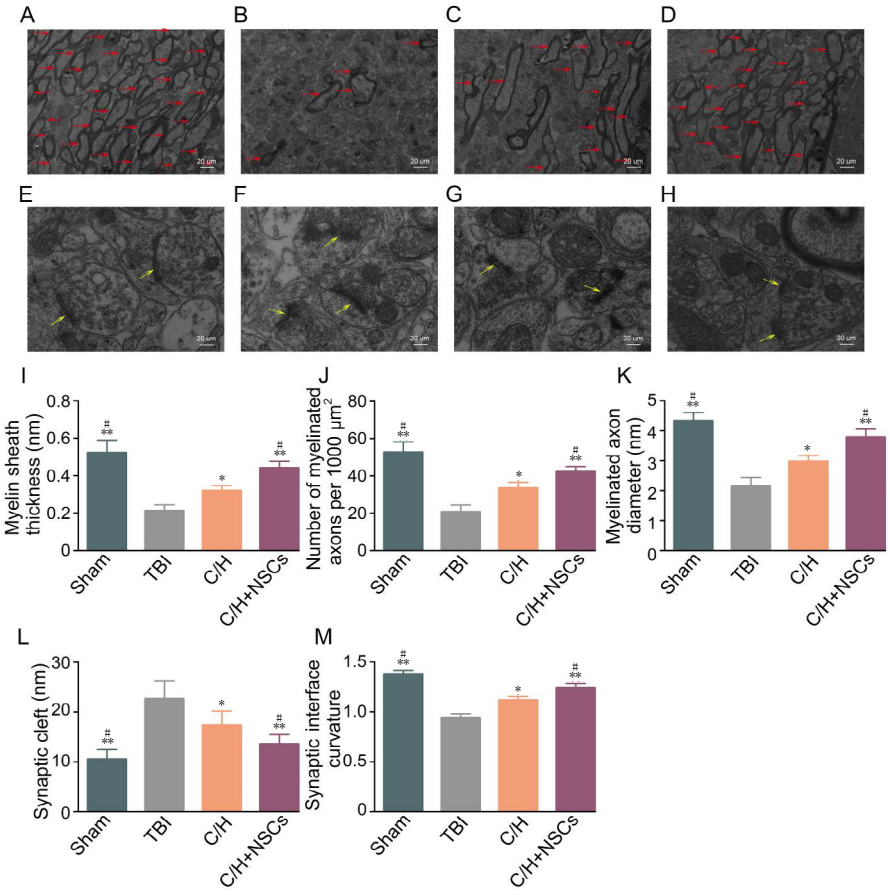

Figure 5 | C/H + NSC therapy promotes the rehabilitation of injured synapses and myelin sheaths after TBI.

(A–H) Representative series of ultrastructural micrographs of synapses and myelin sheaths in the injury site after TBI. (A, E) In the sham group, myelinated axons were normal (A). There were many synaptic vesicles in the presynaptic elements and many dense materials attached to postsynaptic elements. The synaptic cleft was narrow, and the postsynaptic density was centralized (E). (B, F) In the TBI group, the myelinated axon diameter, myelinated thickness, and the number of myelinated axons were significantly decreased compared with the other groups (B). The synaptic cleft was markedly increased with decreased synaptic interface curvature (F). (C, D, G, H) In the C/H (C, G) and C/H + NSCs (D, H) groups, a large number of myelinated axons were observed, and the myelinated axon diameter and myelinated thickness were relatively normal compared with the TBI group (C, D). The C/H + NSCs group showed better synaptic cleft structures and synaptic interface curvature compared with the C/H group. Red arrows indicate myelin sheaths (G, H). Yellow arrows indicate synapses. Scale bars: 20 μm in A–H. (I) The myelinated thickness among the four groups. (J) The number of myelinated axons per 1000 μm^2 among the four groups. (K) The myelinated axon diameter among the four groups. (L) The synaptic cleft among the four groups. (M) The synaptic interface curvature among the four groups. Data are expressed as the mean ± SD. *P < 0.05, **P < 0.01, *vs.* TBI group; #P < 0.05, *vs.* C/H group (one-way analysis of variance followed by the Student-Newman-Keuls test). C/H: Collagen/heparan sulfate; NSC: neural stem cell; TBI: traumatic brain injury.

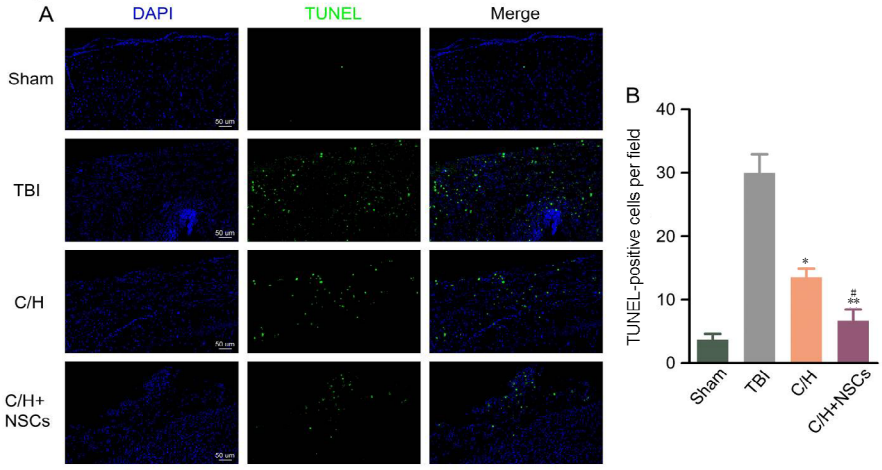

Figure 6 | C/H + NSC therapy inhibits the apoptosis of nerve cells after TBI.

(A) Representative images of TUNEL staining in the perilesional region. The sham group had almost no TUNEL-positive cells. The number of TUNEL-positive cells was significantly higher in the TBI group compared with the C/H and C/H + NSCs groups, and the C/H + NSCs group had fewer TUNEL-positive cells than the C/H group. TUNEL: green; DAPI: blue. Scale bars: 50 μm. (B) Quantification of TUNEL-positive cells. Data are expressed as the mean ± SD. *P < 0.05, **P < 0.01, *vs.* TBI group; #P < 0.05, *vs.* C/H group (one-way analysis of variance followed by the Student-Newman-Keuls test). C/H: Collagen/heparan sulfate; DAPI: 6-diamidino-2-phenylindole; NSC: neural stem cell; TBI: traumatic brain injury; TUNEL: terminal deoxynucleotidyl transferase dUTP nick-end labeling.

Discussion

In the field of biomedical engineering, the regeneration and restoration of nerve tissue can be helped considerably by the transplantation of biomaterial scaffolds loaded with stem cells. A composite scaffold made of biodegradable materials can integrate cells into the central nervous system and brain with defined cellular density, thus delivering stem cells to the injury site to achieve excellent therapeutic effects (Carlson et al., 2016; Jin et al., 2016; Chen et al., 2018).

NSCs have been widely used in the treatment of TBI for their anti-hypoxia, anti-ischemia, and differentiation abilities, which can protect brain tissue from secondary injury and improve cerebral function after TBI (Pang et al., 2017; Clervius et al., 2019; Lee et al., 2019). How to better apply NSC therapies in the clinic is a difficult problem that needs to be addressed. Cell therapy is usually accomplished by smearing cell suspensions alone or as a local injection; however, therapy given this way can induce uneven cell distribution (such as insular deposition), cell necrosis caused by regional ischemia/hypoxia, and cell loss, which leads to poor therapeutic effects (Parr et al., 2008; Mothe et al., 2013). It is therefore important to choose an appropriate cell carrier as an extracellular matrix, for NSC proliferation and differentiation. A previous study has confirmed that a polymer scaffold can promote nerve regeneration through physical connection and chemical induction in rat models of TBI (Leung et al., 2012). In the present study, we designed a similar biomaterial scaffold and investigated the effects of this scaffold loaded with NSCs on nerve regeneration and restoration after TBI in rats. The CCK-8 assay revealed that the C/H scaffold had low immunogenicity and reliable biocompatibility, indicating that it is suitable for transplantation *in vivo*. Furthermore, *in vitro* tests demonstrated that the C/H scaffolds had suitable

pore size and shape, porosity, and pore connectivity, which is conducive to the exchange of nutrients and metabolites for the growth of NSCs, and is also helpful to induce the seeding and proliferation of NSCs. The results of Fourier-transform infrared spectroscopic analysis indicated that the C/H scaffold was composed of various water- and lipid-soluble chemical bonds, thus providing an ideal microenvironment for cell adhesion and growth. The X-ray diffraction analysis showed that the composite scaffold had good crystallinity, which is beneficial to control its biodegradability and improve its stability. Moreover, results of the DSC analysis revealed that the composite scaffold had an ideal thermostability and was suitable for grafting *in vivo*. We therefore proposed that this new composite scaffold might have potential applications in treating TBI. Its beneficial characteristics can be attributed to the excellent biocompatibility of collagen, as well as the ability of heparan sulfate to bind to extracellular proteins to regulate various bioactivities (Lu et al., 2007; Chen et al., 2013). Additionally, NSCs adhering to the scaffold can potentially differentiate into neurons, astrocytes, and oligodendrocytes (Reynolds and Weiss, 1992; McKay, 1997), and these brain cells are similar to the original cells and contribute to rehabilitation after TBI.

A previous study has reported that heparan sulfate easily binds to various proteins because its anion sulfate groups can attract cationic amino acid residues, which are very common in proteins (Leong et al., 2015). The biological characteristics of heparan sulfate may be the main reason that heparan sulfate tends to bind to collagen. We noted that the porosity and water absorption of C/H scaffolds were significantly altered compared with collagen scaffolds, suggesting that heparan sulfate enhances the mechanical properties of collagen. Excellent mechanical properties of biological scaffolds are conducive to NSCs (which are seeded on the scaffold) remaining at the injury site long-term without loss, thus better filling the lesion cavity, regulating the local microenvironment, and mediating the directional growth of newborn nervous tissue (Ogle et al., 2016).

The recovery of neurological motor function is a key indicator for evaluating therapeutic effects after TBI, and is the ultimate goal of clinical treatment. As expected, compared with treatment with C/H scaffolds alone, the C/H + NSCs group had better recovery in locomotor function and in the MEP and MWM tests. These findings suggest that NSC participation can further improve pathophysiological processes after TBI *in vivo* and provide an effective molecular delivery platform for the regeneration of nervous tissue. Nissl bodies are polymers composed of many regularly arranged rough endoplasmic reticulum, free protein bodies, and polynuclear bodies, and are the main place in which neurons synthesize proteins (Li et al., 2020). Our Nissl staining results also indicated a clear trend of neuronal regeneration at the injury site in the C/H + NSCs group. This result might be attributed to the suitable porosity and pore size of the C/H scaffold, which may provide an ideal microenvironment for NSCs to differentiate into neurons. Composite scaffolds not only provide a mechanically efficient support structure, but also induce neurovascular regeneration in targeted tissue by providing biological cues. Ideal composite scaffolds should have a mechanically efficient support structure that is suitable for newborn tissue growth, and should also have the ability to provide biological cues to induce tissue regeneration. In parallel to the *in vivo* experiments, TUNEL staining and TEM observation revealed that C/H + NSC transplantation after TBI promoted neuronal survival, synaptic remodeling, and neuronal axon regeneration. Immunohistochemical staining demonstrated that the number of BrdU-positive cells in the injury site was significantly increased in the C/H + NSCs group compared with the C/H group, indicating that C/H + NSCs therapy can provide an optimal neural circuit repair microenvironment by activating newborn nerve cells. Thus, the neuroprotective effect of C/H + NSC therapy may be superior to that of the C/H scaffold alone. The main reason for this finding is that the C/H scaffold + NSCs can directionally deliver NSCs to the injury site and promote their proliferation in the lesion area, thus avoiding cell loss and inactivation because of a lack of tissue support.

The low regenerative ability of neurons and excessive astrocytic proliferation can lead to neuroinflammatory reactions after TBI, which in turn causes fibrous scarring that inhibits damaged nervous tissue repair. Luo et al. (2019) demonstrated that NSCs stop the inflammatory reaction process by inhibiting astrocyte activation around the damaged area of nervous tissue, thus improving the ability of nerve cells to differentiate into neurons and increasing the expression of growth factors and anti-apoptotic proteins in the host brain. Hayashi et al. (2004) reported that heparans play positive roles in anti-fibrosis and anti-inflammation by preventing interactions between fibroblast growth factors and heparan sulfate glycoproteins on the cell surface. Based on these findings, we hypothesize that the reason that the C/H + NSCs group showed better recovery of sensory and motor functions was closely related to the anti-fibrotic and anti-inflammatory abilities of NSCs and heparan sulfate.

There are some limitations in our study. First, we did not measure the mechanical properties of C/H scaffolds before sterilization. The mechanical properties of most natural biological materials are changed to different degrees after sterilization by ^{60}Co irradiation, because ^{60}Co irradiation induces the denaturation of chemical bonds (Liu et al., 2013). However, the irradiation dose of ^{60}Co in our study was 15 kGy, which is within the safe range (15–25 kGy). Irradiation doses in this range kill viruses or pathogens, but have minimal effects on the biological activity and physicochemical properties of the biomaterials themselves (Li et al., 2007; Wang et al., 2018; Xing et al., 2019). The key points of our study were the processes of C/H scaffolds co-cultured with NSCs and the transplantation of scaffolds into the brain after TBI; these processes were all based on the use of sterilized C/H scaffolds and had little to do with non-sterilized C/H scaffolds. Thus, we initially believed that the mechanical properties of C/H scaffolds before sterilization were irrelevant to the research results, and we did not measure the mechanical properties of C/H scaffolds before ^{60}Co irradiation. Second, a key point in neural tissue engineering involves the ways in which the directional differentiation of NSCs can be regulated, and our research did not address this point well. Leipzig and Shoichet (2009) suggested that NSCs are more likely to differentiate into neurons on the surface of soft hydrogel than on stiff biomaterials, indicating that we may be able to adjust the C/H ratio in the C/H scaffold to find the most suitable ratio for NSCs to differentiate into neurons. This would further promote neurological repair after TBI. Another approach would be to regulate the directional differentiation of NSCs by adding the transcription factor ZEB2 (Deryckere et al., 2020) or gold nanocomposites (Zhang et al., 2020), which both have the ability to induce directional differentiation of stem cells. These aspects will continue to be the focus of future research. In summary, we can confirm that C/H + NSC therapy has the potential for application in neural tissue engineering. We hope to further develop different types of composite scaffolds, such as by loading neurotrophic factors or exosomes to the scaffolds, to provide greater feasibility for clinical application.

Author contributions: *Study conception or design: JZ, RJW; data acquisition, analysis, and interpretation: JZ, MC, KM, HYX, YCY, WXL; manuscript draft: JZ; manuscript revision: RJW, XYL, WSD, XYC; research coordination and integration: XYC, HTS. All authors approved the final version of the paper for publication.*
Conflicts of interest: *The authors declare no conflict of interest.*
Financial support: *This work was supported by the National Natural Science*

Foundation of China, Nos. 11672332, 11932013 (both to XYC); the National Key Research and Development Plan of China, No. 2016YFC1101500 (to HTS); the Key Science and Technology Support Foundation of Tianjin of China, No. 17YFZCSY00620 (to HTS). The funding sources had no role in study conception and design, data analysis or interpretation, paper writing or deciding to submit this paper for publication.

Institutional review board statement: *This study was approved by the Institutional Ethics Committee of Characteristic Medical Center of Chinese People's Armed Police Force, China (approval No. 2017-0007.2) on February 10, 2019.*

Copyright license agreement: *The Copyright License Agreement has been signed by all authors before publication.*

Data sharing statement: *Datasets analyzed during the current study are available from the corresponding author on reasonable request.*

Plagiarism check: *Checked twice by iThenticate.*

Peer review: *Externally peer reviewed.*

Open peer reviewer: *Zachary Campagna Janatpour, Uniformed Services University of the Health Sciences Pharmacology, USA.*

References

Bose S, Roy M, Bandyopadhyay A (2012) Recent advances in bone tissue engineering scaffolds. Trends Biotechnol 30:546-554.

Carlson AL, Bennett NK, Francis NL, Halikere A, Clarke S, Moore JC, Hart RP, Paradiso K, Wernig M, Kohn J, Pang ZP, Moghe PV (2016) Generation and transplantation of reprogrammed human neurons in the brain using 3D microtopographic scaffolds. Nat Commun 7:10862.

Chen C, Zhao ML, Zhang RK, Lu G, Zhao CY, Fu F, Sun HT, Zhang S, Tu Y, Li XH (2017) Collagen/heparin sulfate scaffolds fabricated by a 3D bioprinter improved mechanical properties and neurological function after spinal cord injury in rats. J Biomed Mater Res A 105:1324-1332.

Chen F, Hableel G, Zhao ER, Jokerst JV (2018) Multifunctional nanomedicine with silica: Role of silica in nanoparticles for theranostic, imaging, and drug monitoring. J Colloid Interface Sci 521:261-279.

Chen JP, Chen SH, Lai GJ (2012a) Preparation and characterization of biomimetic silk fibroin/chitosan composite nanofibers by electrospinning for osteoblasts culture. Nanoscale Res Lett 7:170.

Chen L, Xiao Z, Meng Y, Zhao Y, Han J, Su G, Chen B, Dai J (2012b) The enhancement of cancer stem cell properties of MCF-7 cells in 3D collagen scaffolds for modeling of cancer and anti-cancer drugs. Biomaterials 33:1437-1444.

Chen Y, Scully M, Dawson G, Goodwin C, Xia M, Lu X, Kakkar A (2013) Perturbation of the heparin/heparin-sulfate interactome of human breast cancer cells modulates pro-tumourigenic effects associated with PI3K/Akt and MAPK/ERK signalling. Thromb Haemost 109:1148-1157.

Cheng SX, Xu ZW, Yi TL, Sun HT, Yang C, Yu ZQ, Yang XS, Jin XH, Tu Y, Zhang S (2018) iTRAQ-based quantitative proteomics reveals the new evidence base for traumatic brain injury treated with targeted temperature management. Neurotherapeutics 15:216-232.

Clervius H, Baig M, Mahavadi A, Gajavelli S (2019) Human neural stem cell transplants to address multiple pathologies associated with traumatic brain injury. Neural Regen Res 14:1699-1700.

Cornwell KG, Lei P, Andreadis ST, Pins GD (2007) Crosslinking of discrete self-assembled collagen threads: Effects on mechanical strength and cell-matrix interactions. J Biomed Mater Res A 80:362-371.

Cromer Berman SM, Kshitiz, Wang CJ, Orukari I, Levchenko A, Bulte JW, Walczak P (2013) Cell motility of neural stem cells is reduced after SPIO-labeling, which is mitigated after exocytosis. Magn Reson Med 69:255-262.

Deryckere A, Stappers E, Dries R, Peyre E, van den Berghe V, Conidi A, Zampeta FI, Francis A, Bresseleers M, Stryjewska A, Vanlaer R, Maas E, Smal IV, van IWFJ, Grosveld FG, Nguyen L, Huylebroeck D, Seuntjens E (2020) Multifaceted actions of Zeb2 in postnatal neurogenesis from the ventricular-subventricular zone to the olfactory bulb. Development 147:dev184861.

Dombrowski C, Song SJ, Chuan P, Lim X, Susanto E, Sawyer AA, Woodruff MA, Hutmacher DW, Nurcombe V, Cool SM (2009) Heparan sulfate mediates the proliferation and differentiation of rat mesenchymal stem cells. Stem Cells Dev 18:661-670.

Echave MC, Hernáez-Moya R, Iturriaga L, Pedraz JL, Lakshminarayanan R, Dolatshahi-Pirouz A, Taebnia N, Orive G (2019) Recent advances in gelatin-based therapeutics. Expert Opin Biol Ther 19:773-779.

Fischbach C, Kong HJ, Hsiong SX, Evangelista MB, Yuen W, Mooney DJ (2009) Cancer cell angiogenic capability is regulated by 3D culture and integrin engagement. Proc Natl Acad Sci U S A 106:399-404.

Gao W, Zhao Z, Yu G, Zhou Z, Zhou Y, Hu T, Jiang R, Zhang J (2015) VEGI attenuates the inflammatory injury and disruption of blood-brain barrier partly by suppressing the TLR4/NF-κB signaling pathway in experimental traumatic brain injury. Brain Res 1622:230-239.

Gentleman E, Lay AN, Dickerson DA, Nauman EA, Livesay GA, Dee KC (2003) Mechanical characterization of collagen fibers and scaffolds for tissue engineering. Biomaterials 24:3805-3813.

Hayashi N, Miyata S, Kariya Y, Takano R, Hara S, Kamei K (2004) Attenuation of glial scar formation in the injured rat brain by heparin oligosaccharides. Neurosci Res 49:19-27.

Hu K, Zhang W (2019) Collagen as a medical biomaterial in tissue repair, regeneration and reconstruction. Zhongguo Zuzhi Gongcheng Yanjiu 23:317-322.

Jiang J, Dai C, Niu X, Sun H, Cheng S, Zhang Z, Zhu X, Wang Y, Zhang T, Duan F, Chen X, Zhang S (2018) Establishment of a precise novel brain trauma model in a large animal based on injury of the cerebral motor cortex. J Neurosci Methods 307:95-105.

Jiang JP, Liu XY, Zhao F, Zhu X, Li XY, Niu XG, Yao ZT, Dai C, Xu HY, Ma K, Chen XY, Zhang S (2020) Three-dimensional bioprinting collagen/silk fibroin scaffold combined with neural stem cells promotes nerve regeneration after spinal cord injury. Neural Regen Res 15:959-968.

Jin Y, Bouyer J, Shumsky JS, Haas C, Fischer I (2016) Transplantation of neural progenitor cells in chronic spinal cord injury. Neuroscience 320:69-82.

Karlsson J, Emgård M, Gidö G, Wieloch T, Brundin P (2000) Increased survival of embryonic nigral neurons when grafted to hypothermic rats. Neuroreport 11:1665-1668.

Kee N, Sivalingam S, Boonstra R, Wojtowicz JM (2002) The utility of Ki-67 and BrdU as proliferative markers of adult neurogenesis. J Neurosci Methods 115:97-105.

Khatoun A, Asamoah B, Mc Laughlin M (2019) Investigating the feasibility of epicranial cortical stimulation using concentric-ring electrodes: a novel minimally invasive neuromodulation method. Front Neurosci 13:773.

Kim HJ, Han SJ (2017) Anodal transcranial direct current stimulation provokes neuroplasticity in repetitive mild traumatic brain injury in rats. Neural Plast 2017:1372946.

Lee JY, Acosta S, Tuazon JP, Xu K, Nguyen H, Lippert T, Liska MG, Semechkin A, Garitaonandia I, Gonzalez R, Kern R, Borlongan CV (2019) Human parthenogenetic neural stem cell grafts promote multiple regenerative processes in a traumatic brain injury model. Theranostics 9:1029-1046.

Leipzig ND, Shoichet MS (2009) The effect of substrate stiffness on adult neural stem cell behavior. Biomaterials 30:6867-6878.

Leong NL, Arshi A, Kabir N, Nazemi A, Petrigliano FA, Wu BM, McAllister DR (2015) In vitro and in vivo evaluation of heparin mediated growth factor release from tissue-engineered constructs for anterior cruciate ligament reconstruction. J Orthop Res 33:229-236.

Leung GK, Wang YC, Wu W (2012) Peptide nanofiber scaffold for brain tissue reconstruction. Methods Enzymol 508:177-190.

Li F, Jia H, Yu C (2007) ACL reconstruction in a rabbit model using irradiated Achilles allograft seeded with mesenchymal stem cells or PDGF-B gene-transfected mesenchymal stem cells. Knee Surg Sports Traumatol Arthrosc 15:1219-1227.

Li F, Wang X, Zhang Z, Gao P, Zhang X (2019a) Breviscapine provides a neuroprotective effect after traumatic brain injury by modulating the Nrf2 signaling pathway. J Cell Biochem 120:14899-14907.

Li M, Zhao W, Gao Y, Hao P, Shang J, Duan H, Yang Z, Li X (2019b) Differentiation of bone marrow mesenchymal stem cells into neural lineage cells induced by bfgf-chitosan controlled release system. Biomed Res Int 2019:5086297.

Li S, Cong C, Liu Y, Liu X, Kluwe L, Shan X, Liu H, Gao M, Zhao L, Gao X, Xu L (2020) Tiao Geng decoction for treating menopausal syndrome exhibits anti-aging effects likely via suppressing ASK1/MKK7/JNK mediated apoptosis in ovariectomized rats. J Ethnopharmacol 261:113061.

Liu XL, Zhou WR, Wu YH, Cheng Y, Zheng YF (2013) Effect of sterilization process on surface characteristics and biocompatibility of pure Mg and MgCa alloys. Mater Sci Eng C Mater Biol Appl 33:4144-4154.

Lu Q, Zhang S, Hu K, Feng Q, Cao C, Cui F (2007) Cytocompatibility and blood compatibility of multifunctional fibroin/collagen/heparin scaffolds. Biomaterials 28:2306-2313.

Luo ML, Pan L, Wang L, Wang HY, Li S, Long ZY, Zeng L, Liu Y (2019) Transplantation of NSCs promotes the recovery of cognitive functions by regulating neurotransmitters in rats with traumatic brain injury. Neurochem Res 44:2765-2775.

McKay R (1997) Stem cells in the central nervous system. Science 276:66-71.

Mothe AJ, Tam RY, Zahir T, Tator CH, Shoichet MS (2013) Repair of the injured spinal cord by transplantation of neural stem cells in a hyaluronan-based hydrogel. Biomaterials 34:3775-3783.

Murakami K, Tanaka T, Bando Y, Yoshida S (2015) Nerve injury induces the expression of syndecan-1 heparan sulfate proteoglycan in primary sensory neurons. Neuroscience 300:338-350.

Neher MD, Rich MC, Keene CN, Weckbach S, Bolden AL, Losacco JT, Patane J, Flierl MA, Kulik L, Holers VM, Stahel PF (2014) Deficiency of complement receptors CR2/CR1 in $Cr2^{-/-}$ mice reduces the extent of secondary brain damage after closed head injury. J Neuroinflammation 11:95.

Nurcombe V, Cool SM (2007) Heparan sulfate control of proliferation and differentiation in the stem cell niche. Crit Rev Eukaryot Gene Expr 17:159-171.

Ogle BM, Bursac N, Domian I, Huang NF, Menasché P, Murry CE, Pruitt B, Radisic M, Wu JC, Wu SM, Zhang J, Zimmermann WH, Vunjak-Novakovic G (2016) Distilling complexity to advance cardiac tissue engineering. Sci Transl Med 8:342ps313.

Pang AL, Xiong LL, Xia QJ, Liu F, Wang YC, Liu F, Zhang P, Meng BL, Tan S, Wang TH (2017) Neural stem cell transplantation is associated with inhibition of apoptosis, Bcl-xL upregulation, and recovery of neurological function in a rat model of traumatic brain injury. Cell Transplant 26:1262-1275.

Parr AM, Kulbatski I, Zahir T, Wang X, Yue C, Keating A, Tator CH (2008) Transplanted adult spinal cord-derived neural stem/progenitor cells promote early functional recovery after rat spinal cord injury. Neuroscience 155:760-770.

Reynolds BA, Weiss S (1992) Generation of neurons and astrocytes from isolated cells of the adult mammalian central nervous system. Science 255:1707-1710.

Shreiber DI, Barocas VH, Tranquillo RT (2003) Temporal variations in cell migration and traction during fibroblast-mediated gel compaction. Biophys J 84:4102-4114.

Simionescu DT, Lu Q, Song Y, Lee JS, Rosenbalm TN, Kelley C, Vyavahare NR (2006) Biocompatibility and remodeling potential of pure arterial elastin and collagen scaffolds. Biomaterials 27:702-713.

Skop NB, Calderon F, Levison SW, Gandhi CD, Cho CH (2013) Heparin crosslinked chitosan microspheres for the delivery of neural stem cells and growth factors for central nervous system repair. Acta Biomater 9:6834-6843.

Smith RA, Meade K, Pickford CE, Holley RJ, Merry CL (2011) Glycosaminoglycans as regulators of stem cell differentiation. Biochem Soc Trans 39:383-387.

Tam RY, Fuehrmann T, Mitrousis N, Shoichet MS (2014) Regenerative therapies for central nervous system diseases: a biomaterials approach. Neuropsychopharmacology 39:169-188.

Wang N, Xiao Z, Zhao Y, Wang B, Li X, Li J, Dai J (2018) Collagen scaffold combined with human umbilical cord-derived mesenchymal stem cells promote functional recovery after scar resection in rats with chronic spinal cord injury. J Tissue Eng Regen Med 12:e1154-1163.

Wen Z, Xu X, Xu L, Yang L, Xu X, Zhu J, Wu L, Jiang Y, Liu X (2017) Optimization of behavioural tests for the prediction of outcomes in mouse models of focal middle cerebral artery occlusion. Brain Res 1665:88-94.

Xing Y, Shi S, Zhang Y, Liu F, Zhu L, Shi B, Wang J (2019) Construction of engineered myocardial tissues in vitro with cardiomyocyte-like cells and a polylactic-co-glycolic acid polymer. Mol Med Rep 20:2403-2409.

Yan F, Li M, Zhang HQ, Li GL, Hua Y, Shen Y, Ji XM, Wu CJ, An H, Ren M (2019) Collagen-chitosan scaffold impregnated with bone marrow mesenchymal stem cells for treatment of traumatic brain injury. Neural Regen Res 14:1780-1786.

Yang J, Yao Y, Chen T, Zhang T (2014) VEGF ameliorates cognitive impairment in in vivo and in vitro ischemia via improving neuronal viability and function. Neuromolecular Med 16:376-388.

Yannas IV, Tzeranis DS, Harley BA, So PT (2010) Biologically active collagen-based scaffolds: advances in processing and characterization. Philos Trans A Math Phys Eng Sci 368:2123-2139.

Zeng S, Liu L, Shi Y, Qiu J, Fang W, Rong M, Guo Z, Gao W (2015) Characterization of silk fibroin/chitosan 3D porous scaffold and in vitro cytology. PLoS One 10:e0128658.

Zhang Q, Shi B, Ding J, Yan L, Thawani JP, Fu C, Chen X (2019a) Polymer scaffolds facilitate spinal cord injury repair. Acta Biomater 88:57-77.

Zhang S, Hang Y, Wu J, Tang Z, Li X, Zhang S, Wang L, Brash JL, Chen H (2020) Dual pathway for promotion of stem cell neural differentiation mediated by gold nanocomposites. ACS Appl Mater Interfaces 12:22066-22073.

Zhao S, Wang Z, Chen J, Chen J (2015) Preparation of heparan sulfate-like polysaccharide and application in stem cell chondrogenic differentiation. Carbohydr Res 401:32-38.

P-Reviewer: Janatpour ZC; C-Editor: Zhao M; S-Editors: Yu J, Li CH; L-Editors: Gardner B, Song LP; T-Editor: Jia Y